Modeling and Intelligent-ANFIS Control Design for Fast EV Charging Based on Isolated AC-DC Converter Enhancement with Modular Four-Channel 50 kW WPT System

Dr. J. Srinu Naick, Professor, EEE Department, Chadalawada Ramanamma Engineering College, Tirupati, Andhra Pradesh, India, speaksrinu@gmail.com.

K. Lakshmi Priyanka, B.Tech. Student, EEE Department, Chadalawada Ramanamma Engineering College Tirupati, Chittoor, Andhra Pradesh, India.

Abstract— This paper presents a four-channel WPT system with quick responses and flexibility for EV charging and battery testing. The fast-current converter can simulate on-road power flow by managing battery current in the lab. The four-channel system increases dependability and durability by producing 50 kW of output power with low-power Silicon components. The four-channel magnetic coupler separates channels based on coil layout and construction, which lowers interference, streamlines the control algorithm, and supports modular design. Due to the rotational symmetry of the four-channel magnetic coupler, lateral and vertical misalignment is possible. The battery of an electric vehicle tracks the current command while it is travelling. An AC-DC converter in single-phase mode is used for charging. It transforms into a DC-AC converter to recover battery power. Battery charging and discharging are handled by an additional DC-DC converter. A high-cutoff-frequency LC filter is mounted in front of the battery when the device is in charging mode to lessen voltage ripple. To lower the ripple current in the batteries, a 2 kHz current controller is used. We introduce ANFIS controllers for the rapid, effective, and flexible regulation of PWM-regulated ac/dc converters. In comparison to standard PI controllers, ANFIS controllers offer a stronger transient response.

Keywords: EV charging, AC-DC converter, DC-DC converter, ANFIS controllers, wireless power transfer.

I. INTRODUCTION

The electric vehicle (EV) business has expanded globally in recent years as a result of energy scarcity and environmental degradation. However, there are still some major issues with EVs. For instance, EV batteries take longer to charge than gasoline-powered cars [1], and conventional conductive charging of EVs requires thick gauge cables that are hazardous and difficult to manage. The advantages of aesthetics, safety, convenience, and completely automated charging processes have made wireless power transfer (WPT), which mostly refers to inductive power transfer (IPT), a popular alternative to conductive charging in recent years [2]. Long charging periods are still an issue for WPT, particularly in some real-world applications, such as charging for public transportation systems (buses and electric locomotives) [3]. The key to lowering lengthy charging periods is high-power charging [4]. As a result, there is a growing need for high-power WPT [3], [5,] [6]. It is difficult to enhance the power capabilities of WPT systems because of the voltage and current restrictions on power electronic equipment. High-power WPT systems with a power output of 50 kW or greater have been proposed by certain commercial and academic institutions [7]fi[9], at the expense of employing wide-bandgap technologies like

Silicon-Carbide (SiC). However, devices will continue to be a constraint on system power capability increase. The voltage stress and insulation of resonant parts are additional barriers to the use of high-power wireless charging in the context of the constrained interior volume of EVs in real-world applications. Numerous solutions have been put forth to get around the device and resonant element limits and increase the power capacity of the WPT system in order to solve the aforementioned issue. To increase the power level of the WPT system, a cascaded multilayer inverter is suggested [10] [13]. However, the multilayer converter's cascaded structure suffers. Due to the inverters' series connection, low reliability. The transmitter current can be increased and the WPT system's reliability can be increased by connecting many inverters with low-current semiconductor devices in parallel [14].

 DOI : 10.35291/2454-9150.2022.0388

Insulation design is made more challenging by the high transmitter current's impact on the resonant parts' high voltage stress. There is only one power transfer channel in the system as a result of the one transmitting coil used in both the cascade and parallel connection methods that were previously stated. All of them struggle with malfunction and poor performance when The error happens. In [15]fi[19], the WPT systems with multiple power transfer channels and numerous transmitters and receivers are presented. The voltage stress of the resonant parts and the current stress of the power devices are decreased while the system power capability is increased. However, the amount of cross-coupling between different power transfer channels is low, which leads to uneven power distribution and circulation among channels and significantly reduces the capacity and efficiency of power transfer [15]. In [17], polarised and nonpolarized coils are combined to achieve the decoupling of two magnetic couplers. However, the two-channel system can only transmit 4.73 kW, and because the method cannot be extended, it is not possible to further increase the transmission power capabilities through modularization. In [18] and [19], the magnetic coupling between couplers is eliminated by adjusting the relative positions of the two magnetic couplers built of polarised coils. The transmission powers of the two-channel systems are 44 kW and 7 kW, respectively. The approach is scaleable, but as the number of modules grows, low space utilisation will become an issue. The aforementioned multi-channel systems also experience an imbalance of system misalignment tolerance in the lateral and vertical directions as a result of the peculiarities of polarised coils, which adds to the complexity of EV parking in actual use.

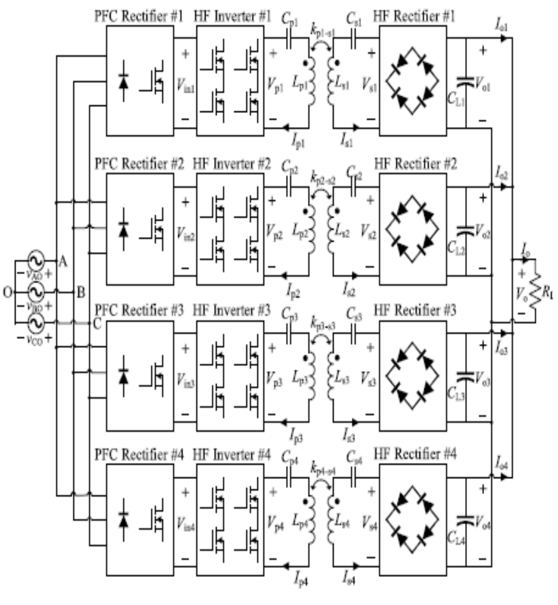

Fig. 1 Block diagram of modular four-channel WPT system.

The four-channel modular WPT system with for quick EV charging, a decoupled coil design is suggested. A primary PFC rectifier, an inverter, a pair of transmitter coils and receiver coils, a secondary rectifier, and a pair of receiver coils are all included in each of the four identical parallel power transfer channels that make up each of the entire WPT modules found in the modular system. The total transferred power is equal to the sum of the power capacities of all modules. modules. The contributions of this paper are summarized as follows. A 50-kW WPT system uses low-power silicon-based devices thanks to modular architecture, which reduces voltage stress on resonant elements. Four identical, distinct channels increase system reliability and resilience.

A four-channel inter-channel decoupled magnetic coupler is proposed; this structure avoids channel interference, simplifies control logic, and enables scalable modular design. The magnetic coupler's rotational symmetry balances the system's tolerance to lateral and vertical misalignment. A Vienna PFC rectifier and cascaded twin full-bridge inverters are suggested to power the transmission coils. This reduces voltage stress on power devices to half the DC bus voltage. The Vienna rectifier has a natural midpoint compared to existing ways for using cascade inverters to create high power [1, 10, 11, 20], and balanced input voltage of each inverter can be achieved. This paper is organized as follows. In Section II, the structure of the modular four-channel WPT system is illustrated, and the input and output characteristics of the system are derived. In Section III, the four-channel decoupled magnetic coupler is designed, and its performance is analysed. In Section IV, the modular circuit is designed. In Section V, the experimental results for the verification of the proposed system are presented. In Section VI, the conclusions are given.

II. MODULAR FOUR-CHANNEL WPT SYSTEM

Fig. 1 displays the block diagram of the proposed modular four-channel WPTsystem, and Table 1 displays the system parameters. The suggested system uses a topology known as input-parallel output-parallel (IPOP), which parallelizes four identical WPT channels. Each channel is a fully functional WPT module that consists of a secondary side high-frequency rectifier, a grid side PFC rectifier, a primary side high-frequency inverter, and compensation networks. The modular architecture is scalable, allowing for the integration of more modules to increase power capability. The development of a generalised modular model with N channels will come next (N is an arbitrary number). For compensating, the SS topology [21, 22] is used. According to these resonance circumstances,

$$\omega_0 = 2\pi f_0 = \frac{1}{\sqrt{L_{pi}C_{pi}}} = \frac{1}{\sqrt{L_{si}C_{si}}} \quad (i = 1, 2, \ldots, N), \tag{1}$$

 DOI : 10.35291/2454-9150.2022.0388

where !0 is the system frequency in rad/s. In accordance with SAE J2954 standard [23], the proposed system operating frequency f0 is 85 kHz. The compensation networks can be compactly represented by matrixes given by

$$\begin{aligned} \underline{\mathbf{L}}_{\mathrm{p}} &= \mathrm{diag}[L_{\mathrm{p}1}L_{\mathrm{p}2}...L_{\mathrm{p}N}] \\ \underline{\mathbf{L}}_{\mathrm{s}} &= \mathrm{diag}[L_{\mathrm{s}1}L_{\mathrm{s}2}...L_{\mathrm{s}N}] \\ \underline{\mathbf{C}}_{\mathrm{p}} &= \mathrm{diag}[C_{\mathrm{p}1}C_{\mathrm{p}2}...C_{\mathrm{p}N}] \\ \underline{\mathbf{C}}_{\mathrm{s}} &= \mathrm{diag}[C_{\mathrm{s}1}C_{\mathrm{s}2}...C_{\mathrm{s}N}], \end{aligned} \quad (2)$$

Lp and Ls are multi-channel inductance matrixes, Cp and Cs are multi-channel capacitance matrixes. ZLp = jωLp, ZLs = jωLs, ZCp = $(j\omega Cp)^{-1}$ and ZCs = $(j\omega Cp)^{-1}$ are linked to the inductance and capacitance matrices by the impedance matrices. The fundamental approximation is used to assess the key characteristics of the proposed modular topology.The multi-channel primary and secondary coil currents are represented by the current vectors while high order harmonics are ignored. Ip = $[Ip1\ Ip2: :: IpN]^{T}$ and Is = $[Is1Is2: :: IsN]^{T}$ respectively. The multi-channel output current and voltage are given by vectors Io = $[Io1\ Io2: :: IoN]^{T}$ and Vo = $[Vo1Vo2: :: VoN]^{T}$ respectively. The input and output voltage of multi-channel inverters and the input voltage of the secondary rectifiers are given by vectors Vin = $[Vin1Vin2: :: VinN]^{T}$, Vp = $[Vp1Vp2: :: VpN]^{T}$, and Vs = $[Vs1Vs2: :: VsN]^{T}$ respectively. Consider the mutual inductance matrix M between multi-channel primary and secondary coils, the equivalent load matrix Rac observed before secondary rectifiers are given by, as well as the crosscoupling between channels[19].

$$\underline{\mathbf{M}}_{\mathrm{p-s}} = \begin{bmatrix} M_{\mathrm{p1-s1}} & M_{\mathrm{p1-s2}} & \cdots & M_{\mathrm{p1-s}N} \\ M_{\mathrm{p2-s1}} & M_{\mathrm{p2-s2}} & \cdots & M_{\mathrm{p2-s}N} \\ \vdots & \vdots & \ddots & \vdots \\ M_{\mathrm{p}N\mathrm{-s1}} & M_{\mathrm{p}N\mathrm{-s2}} & \cdots & M_{\mathrm{p}N\mathrm{-s}N} \end{bmatrix} \quad (3)$$

$$\underline{\mathbf{M}}_{\mathrm{p-p}} = \begin{bmatrix} 0 & M_{\mathrm{p1-p2}} & \cdots & M_{\mathrm{p1-p}N} \\ M_{\mathrm{p2-p1}} & 0 & \cdots & M_{\mathrm{p2-p}N} \\ \vdots & \vdots & \ddots & \vdots \\ M_{\mathrm{p}N\mathrm{-p1}} & M_{\mathrm{p}N\mathrm{-p2}} & \cdots & 0 \end{bmatrix} \quad (4)$$

$$\underline{\mathbf{M}}_{\mathrm{s-s}} = \begin{bmatrix} 0 & M_{\mathrm{s1-s2}} & \cdots & M_{\mathrm{s1-s}N} \\ M_{\mathrm{s2-s1}} & 0 & \cdots & M_{\mathrm{s2-s}N} \\ \vdots & \vdots & \ddots & \vdots \\ M_{\mathrm{s}N\mathrm{-s1}} & M_{\mathrm{s}N\mathrm{-s2}} & \cdots & 0 \end{bmatrix} \quad (5)$$

Rac D diag[Rac1Rac2: : :RacN]: (6)

Using the fundamental approximation, define

$$\mathbf{V}_{\mathrm{p}} = \frac{4}{\pi}\mathbf{V}_{\mathrm{in}}, \quad \mathbf{V}_{\mathrm{s}} = \frac{4}{\pi}\mathbf{V}_{\mathrm{o}}. \quad (7)$$

From Fig. 1, Kirchhoff's voltage law gives

$$\mathbf{V}_{\mathrm{p}} = (\underline{\mathbf{Z}}_{Lp} + \underline{\mathbf{Z}}_{Cp})\mathbf{I}_{\mathrm{p}} + j\omega_0\underline{\mathbf{M}}_{\mathrm{p-s}}\mathbf{I}_{\mathrm{s}} + j\omega_0\underline{\mathbf{M}}_{\mathrm{p-p}}\mathbf{I}_{\mathrm{p}} \quad (8)$$

$$j\omega_0\underline{\mathbf{M}}_{\mathrm{p-s}}\mathbf{I}_{\mathrm{p}} + j\omega_0\underline{\mathbf{M}}_{\mathrm{s-s}}\mathbf{I}_{\mathrm{s}} = -(\underline{\mathbf{Z}}_{Ls} + \underline{\mathbf{Z}}_{Cs})\mathbf{I}_{\mathrm{s}} - \underline{\mathbf{R}}_{\mathrm{ac}}\mathbf{I}_{\mathrm{s}}. \quad (9)$$

Substituting (1) into (8) and (9), then

$$\mathbf{V}_{\mathrm{p}} = j\omega_0\underline{\mathbf{M}}_{\mathrm{p-s}}\mathbf{I}_{\mathrm{s}} + j\omega_0\underline{\mathbf{M}}_{\mathrm{p-p}}\mathbf{I}_{\mathrm{p}} \quad (10)$$

$$j\omega_0\underline{\mathbf{M}}_{\mathrm{p-s}}\mathbf{I}_{\mathrm{p}} + j\omega_0\underline{\mathbf{M}}_{\mathrm{s-s}}\mathbf{I}_{\mathrm{s}} = -\underline{\mathbf{R}}_{\mathrm{ac}}\mathbf{I}_{\mathrm{s}}. \quad (11)$$

The multi-channel secondary coil current vector can be calculated as

$$\mathbf{I}_{\mathrm{s}} = \frac{\underline{\mathbf{M}}_{\mathrm{p-s}}\mathbf{V}_{\mathrm{p}}}{j\omega_0\underline{\mathbf{M}}^2_{\mathrm{p-s}} - (j\omega_0\underline{\mathbf{M}_{\mathrm{p-p}}\mathbf{M}_{\mathrm{s-s}}} + \underline{\mathbf{M}}_{\mathrm{p-p}}\underline{\mathbf{R}}_{\mathrm{ac}})}. \quad (12)$$

In consideration of the rectifier bridge, the output dc current vector can be estimated as

$$\mathbf{I}_{\mathrm{o}} = \frac{2\sqrt{2}}{\pi}\mathbf{I}_{\mathrm{s}}. \quad (13)$$

Combining (7)(12) and (13), the output current of each channel can be expressed as

$$\mathbf{I}_{\mathrm{o}} = \frac{8\sqrt{2}\mathbf{V}_{\mathrm{in}}}{j\pi^2\omega_0\underline{\mathbf{M}}_{\mathrm{p-s}} - (j\pi^2\omega_0\frac{\mathbf{M}_{\mathrm{p-p}}\mathbf{M}_{\mathrm{s-s}}}{\underline{\mathbf{M}}_{\mathrm{p-s}}} + \frac{\mathbf{M}_{\mathrm{p-p}}}{\underline{\mathbf{M}}_{\mathrm{p-s}}}\underline{\mathbf{R}}_{\mathrm{ac}})} = \underline{\mathbf{G}}\mathbf{V}_{\mathrm{in}}, \quad (14)$$

where G is the multi-channel input to output gain matrix. According to (14), when there is cross-coupling between channels, each channel's output is affected by other channels rather than being independent, which affects the ZVS's operation and power transfer capacity and makes the control logic more difficult. G transforms into a diagonal matrix and each channel output behaves as a separate current source when the multi-channel system has interchannel decoupling, on the other hand[20]. As a result, Vo1 = Vo2…= VoN = Vo can be obtained by parallelizing the output of the various channels. Additionally, the comparable circuit model depicted in Fig. 2 can be used to define the proposed multi-channel WPT system. The output power of the multi-channel system is Io1 = Io2…= IoN when each channel output is balanced.

$$P_{\mathrm{o}} = V_{\mathrm{o}}I_{\mathrm{o}} = V_{\mathrm{o}}\left(I_{\mathrm{o}1} + I_{\mathrm{o}2}...+I_{\mathrm{o}4}\right), \quad (15)$$

and the equivalent DC load relationship of each channel is

$$R_{\mathrm{L}1} = R_{\mathrm{L}2}...= R_{\mathrm{L}N} = \frac{V_{\mathrm{o}}}{I_{\mathrm{o}}/N} = NR_{\mathrm{L}}. \quad (16)$$

The equivalent DC load of each channel is represented as RL1 RLN, where RL represents the actual load connected to the multi-channel system. According to (15), the four-channel system's overall transmission power capacity is four times greater than that of the single-channel system[21][22]. Therefore, it may be concluded that, at the same power level, the four-channel system's current stress on power devices is one-fourth that of the conventional single-channel system. The modular design has the following benefits for high-power WPT applications like quick EV charging. First off, the four-channel structure at the same power level allows the use of

 DOI : 10.35291/2454-9150.2022.0388

low power components, which are normally simpler to produce, and the voltage stress of the resonant elements is comparatively low compared to the single-channel structure. Second, a full redesign of the power supply might be required to increase power level in a single-channel system. By paralleling various module numbers, on the other hand, adjustable power levels can be achieved. Third, the system's four identical channels can function independently, greatly enhancing the WPT system's dependability and resilience. Fourth, because the heat produced is distributed more evenly, the modular construction simplifies the thermal design of the system.

III. SIMULATION OF COUPLING COEFFICIENT AND MISALIGNMENT

The suggested four channel magnetic coupler simulation is run using 3-D FEM to confirm the inter-channel decoupling. The four-channel magnetic coupler has eight inductive coils (Lp1 ~Lp4 and Ls1 ~Ls4), which allows for the formation of a total of 28 coupling coefficients, including four for power transmission (kp1–s1, kp2-s2, kp3–s3, and kp4–s4) and 24 for interference (kpi–sj, kpi–pj, and ksi–sj (i–j)). The simulation results of the coupling coefficients between the primary coil Lp1 and the other 7 coils for the case where the primary and secondary sides of the magnetic coupler are horizontally aligned and the air gap Hgap is 200 mm. The 7 coupling coefficients of the primary coil Lp1 can be used to express all 28 coupling coefficients in the magnetic coupler since it is symmetrical about the centre. The simulation results in Table 3 demonstrate that the coupling coefficient kp1-s1 for power transmission is 0.261 when the primary and secondary sides are horizontally aligned, while the six interference coupling coefficients between the channels are two orders of magnitude smaller than kp1-s1, or roughly zero[23].

As a result, the four-channel magnetic coupler is designed to achieve inter-channel decoupling under aligned conditions. The suggested four-channel magnetic coupler's misalignment performance is also examined, including the coupling coefficient between primary coil Lp1 and the other seven coils under various misalignment conditions. A zero-coupling point is given in the lateral direction (X-axis) at an offset of about 34% of the coil dimension because of the structural properties of the == coupler [25]. The performance of the single-channel coupler's ant misalignment is significantly better in the vertical (Y-axis) direction than in the lateral direction (X-axis). The coupling coefficient for power transmission reduces dramatically to virtually zero when the lateral (X-axis) misalignment reaches 200 mm. The conventional single-channel system with DD coils is unable to transmit power effectively in this situation. The system output power under misalignment situations is investigated by simulation in order to compare the misalignment performance of a four-channel magnetic coupler with a single-channel coupler. It should be noted that because of the properties of the SS topology, misalignment causes a decrease in coupling coefficient and an increase in power coil current, which may be more than the coil's current capacity. As a result, the system's output power is calculated using the same primary coil current in an aligned state. In actuality, these circumstances cause the output power to drop. It can be inferred that the magnetic coupler has rotational symmetry and a 90° rotation angle thanks to the design of the arrangement of the four-channel coils. As a result, both the lateral (X-axis) and vertical misalignment tolerances of the proposed four-channel magnetic coupler are equal (Y-axis). The simulation findings show that the proposed modular four-channel system has a balanced tolerance to misalignment in both the lateral and vertical dimensions as compared to the conventional single-channel system with DD coils. A collaborative simulation using 3-D FEM and ANSYS Implorer is used to confirm the operational performance of the four-channel magnetic coupler that was designed.

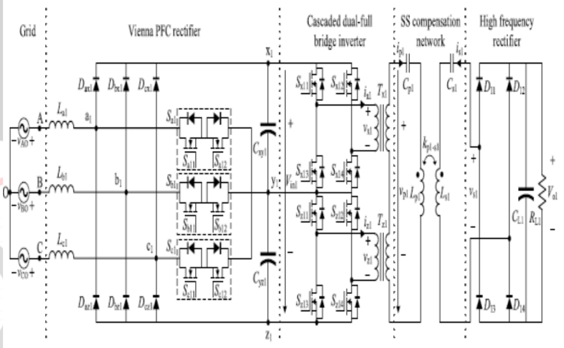

Fig. 2 Schematic diagram of the circuit module.

It is determined what the magnetic field is surrounding the four channel coils. The operating circumstances of each channel can be described by the magnetic field distribution around the two neighboring channel coils thanks to the four-channel magnetic coupler's rotational symmetry. The 3-D model of the four channel coils defines a 2-D cut surface. the magnetic field on the cut surface at various levels of misalignment. The provided power of the channel on the left is found to dramatically drop with an increase in misalignment, while the delivered power of the channel on the right remains high, which is consistent with the theoretical explanation.

Using Channel 1 as an example, Fig. 2 displays the experimental waveform for Channel 1 at full load. The cascaded dual-full bridge inverter's higher inverter's output voltage is vx1, the lower inverter's output voltage is vz1, the upper inverter's output current is ix1, and the secondary side's output voltage is Vo1[25]. The single-channel rated load RL1 42 is the load, and the inverter input voltage Vin1 is 750 V. As can be observed, the output voltages of the upper and lower inverters are identical (vx1 and vz1, respectively). The ZVS is realised

 DOI : 10.35291/2454-9150.2022.0388

because ix1's peak value is 30 A and vx1's phase is just a little bit ahead of ix1's (iz1) phase. The output power of Channel 1 is 12.9 kW, while the secondary output voltage Vo1 is 736 V. The efficiency of the system's dc-to-dc transmission is written as

$$\eta = \frac{P_{out}}{P_{in}} = \frac{V_o \sum_{i=1}^{4} I_{oi}}{\sum_{i=1}^{4} V_{ini} I_{ini}}. \quad (17)$$

IV. MODULAR CIRCUIT DESIGN

The proposed four-channel WPT system contains a circuit module for each channel with the identical characteristics, as shown in Fig. 1. A grid-side PFC rectifier, a primary side high-frequency inverter, compensation networks, and a secondary side high-frequency rectifier are all components of the circuit module. The circuit module's schematic is displayed in Fig. 10 using Channel 1 as an example.

A. RECTIFIER FOR GIRD-SIDE PFC

Vienna rectifier is used as the grid-side rectifier. Small passive components size, high power density, and high rectification efficiency are characteristics of the Vienna rectifier [26]. The rectifier is able to provide a greater DC voltage output because its voltage stress (Vin1 in Fig. 10) is only half that of its output DC voltage. The high-voltage DC bus helps to reduce power coil current in the circuit's later stages. When the power coil's quality factor is set, the loss of the power coil is reduced, and the effectiveness of energy transmission is increased. The explanation of the Vienna rectifier's operating mode and control scheme is outside the purview of this paper's research. As illustrated in Fig. 11, the output of the Vienna rectifier can be equivalent to two series DC voltage sources of similar amplitude, which will make it easier to understand the post-stage circuit. The voltage relationship is as follows.

$$V_{\mathrm{xy1}} = V_{\mathrm{yz1}} = \frac{1}{2} V_{\mathrm{in1}}. \quad (18)$$

B. PRIMARY SIDE HIGH-FREQUENCY INVERTER

The current capacity of the power devices in the inverter in the proposed modular four-channel system is one-fourth of at the same power level as the single-channel system. A cascaded dual-full bridge inverter is used, as shown in Fig., to simultaneously lower the voltage stress on the devices. 10. The DC sources Vxy1 and Vyz1 in Fig. are the input sources for the two full-bridge inverters. 11, or 50 percent of the Vin1 DC bus voltage. In comparison to the conventional full-bridge inverter, the cascaded design cuts the voltage stress on power electronics in half. Therefore, a cost-effective solution for the 800 V DC bus voltage is to employ silicon-based MOSFETs with a 650 V withstand voltage in Vienna rectifiers and inverters. In this study, it is shown that the same voltage level may be achieved by Si devices by combining Vienna rectifier and cascaded inverter, whereas typically, a single inverter needs SiC devices to provide an input and output voltage level of 800 V. Furthermore, compared to the current methods of using cascade inverters to achieve high power, the problem of device damage caused by inconsistent voltage stress of the inverter's switching devices is avoided with the combination of Vienna PFC rectifier and cascaded dual full-bridge inverters because the output of the Vienna rectifier has a natural midpoint. The output of the upper and lower inverters cannot be cascaded directly because the two input voltage sources Vxy1 and Vyz1 of the cascaded dual-full bridge inverter are not two isolated sources because they share a point y1. Instead, the high-frequency transformers Tx1 and Tz1 cascade the upper and lower inverter's output instead (turn ratio 1:1). Otherwise, the DC voltage sources Vxy1 and Vyz1 would be short-circuited in some switching states. The electrical isolation between the inverter and the post-stage circuit is another advantage of using high-frequency transformers. The two full-bridge inverters' switch driving signals are configured to be consistent. As a result, the output voltage of the cascaded dual-full bridge inverter, vp1, is double that of a single full-bridge inverter, vx1 or vz1.

$$v_{\mathrm{p1}} = 2v_{\mathrm{x1}} = 2v_{\mathrm{z1}} \quad (19)$$

$$i_{\mathrm{p1}} = i_{\mathrm{x1}} = i_{\mathrm{z1}} \quad (20)$$

For the Vienna rectifier and cascaded dual-full bridge inverter, an Infineon IPW65R080CFD 650 V/27 A silicon-based MOSFET was chosen. The device's rated 650 V voltage offers enough margin for half of the 400 V maximum DC bus voltage. To achieve minimal conduction losses, the dual-full bridge inverter uses two parallel-connected components with 80 m ON-state resistance in TO-247 housings for each switch.

V. NEW PROPOSED CONTROL TECHNIQUE

The membership function parameters of a fuzzy inference system are tuned (adjusted) using either a back-propagation algorithm alone, or in combination with a least squares type of method, in an adaptive neuro-fuzzy inference strategy that utilises a given input/output data set. The input/output map can be interpreted using a network-type structure, comparable to a neural network, that maps inputs through input membership functions and related parameters, and then maps outputs through output membership functions and associated parameters. Figure.4 illustrates the fundamental organisation of the ANFIS algorithm using a first order Sugeno-type fuzzy system.

 DOI : 10.35291/2454-9150.2022.0388

ISSN : 2454-9150 Vol-08, Issue-04, July 2022

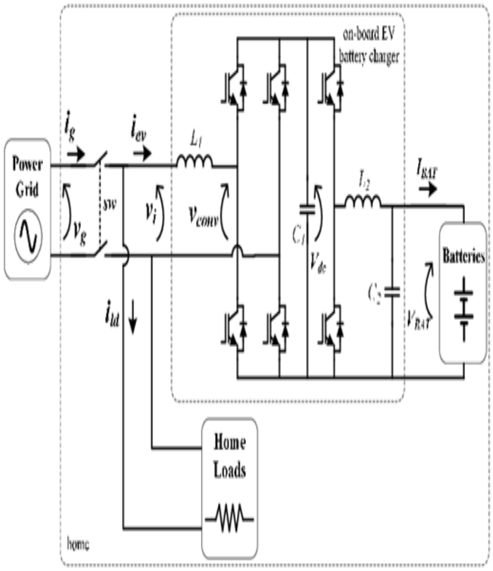

Fig. 3 Proposed topology of the battery charger and the setup that was used to obtain

The linguistic control strategy based on expert knowledge is transformed into a controller strategy using a fuzzy logic controller (FLC), which applies fuzzy logic. The Takagi-Sugeno-Kang or Sugeno methods of fuzzy inference have been applied in this work. Consequently, we first go over some foundational concepts for fuzzy inference systems (FIS). Fuzzy rule-based systems, fuzzy models, and fuzzy controllers are other names for FIS (when used as controllers). Fuzzy logic requires the addition of a front-end "fuzzifier" and a rear-end "defuzzifier" to the standard input-output data set in order to be used for control. Rule base, fuzzifier, inference engine, and defuzzifier are the four parts of a straightforward FLC. It can be viewed as a nonlinear mapping from the input to the output once the rules have been set. These guidelines may come directly from experts, but if no experts are available, they can alternatively be derived by properly analysing the given input output data (for example, clustering).

A FIS consists of five functional blocks as shown in Fig. 5. A rule base, containing a number of fuzzy if-then rules. A data base, which defines the membership functions of the fuzzy sets used in the fuzzy rules. A decision-making unit, which performs the inference operations on the rules. A fuzzification interface, which transforms the crisp inputs into degrees of match with linguistic values. A defuzzification interface, which transforms the fuzzy results into a crisp output. Generally, the rule base and data base are jointly referred to as the knowledge base.

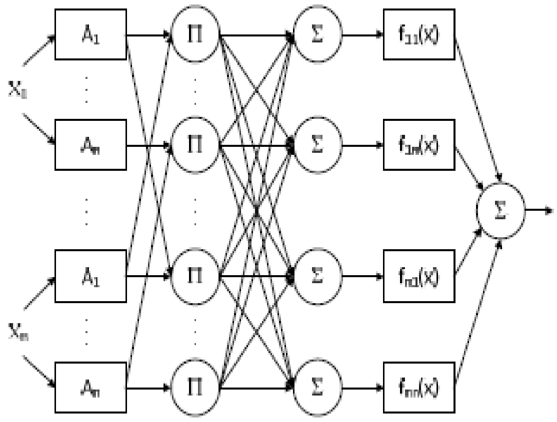

Fig. 4 Typical ANFIS structure

The Mamdani-type and the Sugeno-type are the two different categories of fuzzy inference systems. The methods used to determine outputs in these two categories of inference systems differ somewhat. The most popular fuzzy approach is Mamdani's fuzzy inference method. Mamdani-type inference anticipates fuzzy sets for the output membership functions. The centroid of a two-dimensional aggregate output function is located in order to defuzzify the fuzzy sets that remain after the aggregation procedure for each output variable. The Sugeno method of fuzzy inference, which was first developed in 1985, shares many characteristics with the Mamdani approach. Fuzzifying the inputs and using the fuzzy operator are the first two steps in the fuzzy inference process, and they are identical. Sugeno's approach differs significantly from Mamdani's in that the output membership functions are either linear or constant. Returning to Fig. 2, we now provide a conceptual explanation of the ANFIS operation and layers.

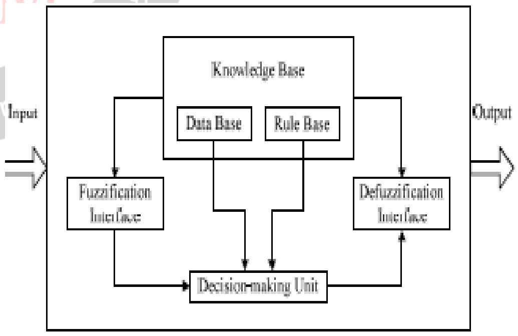

Fig. 5 Block diagram of a fuzzy inference system

Layer 1: The input to node I in this layer is represented as a square node with the node function O i' = (A i) (x), where A i is the linguistic label (small, large, etc.) connected to this node function. O i', or the membership function of A i, describes the extent to which the provided x satisfies the quantifier A i. Typically, _(A i) (x) is chosen to be bell-shaped, with a maximum value of 1 and a minimum value of 0, as in

$$\mu_{A_i}(x) = \left\{1+\left[\left(\frac{x-c_i}{a_i}\right)^2\right]^{b_i}\right\}^{-1} \quad or \quad \mu_{A_i}(x) = \exp\left\{-\left(\frac{x-c_i}{a_i}\right)^2\right\} \qquad (21)$$

 DOI : 10.35291/2454-9150.2022.0388

ISSN : 2454-9150 Vol-08, Issue-04, July 2022

where $\{a_i, b_i, c_i\}$ is the parameter set of the bell function. In fact, any piecewise differentiable function, such as a trapezoidal or a triangular-shaped membership function, is also a qualified candidate for node functions in this layer. Parameters in this layer are referred to as premise parameters.

Layer 2: Every node, in this layer, is denoted as a circle node, labeled Π, which multiplies the incoming signals and sends the product out. Each output node represents the firing strength of a rule. In fact, other T-norm operators that perform the generalized AND function can be used as the node function in this layer.

Layer 3: Every node in this layer is also shown as a circle, labeled Σ. The ith node calculates the ratio of the ith rule's firing strength to the sum of all rule's firing strengths, such as,

$$\overline{w}_i = \frac{w_i}{\sum_{j=1}^{n} w_j}, i = 1, 2, .., n \tag{22}$$

The outputs of this layer are known as normalized firing strengths.

Layer 4: Every node i in this layer is shown as rectangular with a node function,

$$O_i^4 = \overline{w}_i f_i = \overline{w}_i (p_i x + q_i y + r_i) \tag{23}$$

where w_i is the output of layer 3, and $\{p_i, q_i, r_i\}$ is the parameter set of the Sugeno-type inference system. Parameters in this layer will be referred to as consequent parameters.

Layer 5: The single node in this layer is a circle node labeled Σ that computes the overall output as the summation of

all incoming signals, i.e.,

$$O^5 = \sum_i \overline{w}_i f_i = \frac{\sum_i w_i f_i}{\sum_i w_i} \tag{24}$$

ANFIS employs least mean squares estimation to ascertain the resulting parameters and back propagation learning to learn the parameters associated with membership functions. Each step in the learning process has two components[24]. An iterative least mean squares approach is used to propagate the input patterns and estimate the best subsequent parameters. For the current cycle through the training set, the premise parameters are taken to be fixed. The pattern is repeated, and during this epoch (iteration), back propagation is employed to change the parameters for the premises while keeping the parameters for the consequences fixed. Using a gradient vector, the membership function parameters will evolve during the learning process. After obtaining the gradient vector, several of the available optimization techniques can be used to change the parameters and lower some error measures (usually defined by the sum of the squared difference between actual and desired outputs)[25].

VI. RESULTS AND DISCUSSION OF NEW PROPOSED CONTROL TECHNIQUE

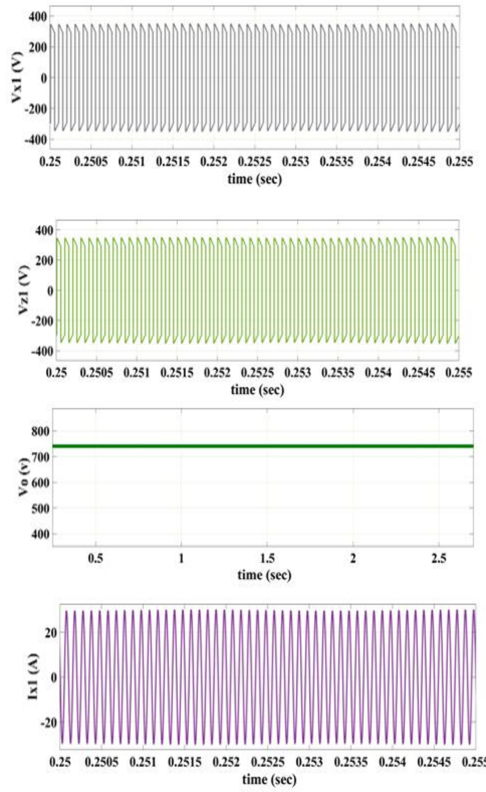

Fig. 6 Waveform when single channel is fully loaded (single-channel load RL1 42 Ω).

97.2 percent of the single-channel efficiency is measured. ix2, ix3, and ix4 are the upper inverter output currents of Channels 2 through 4, respectively; Vo is the four-channel system's output voltage; Fig. 6 displays the experimental waveform with all four channels fully loaded. The four channels' input voltages Vin1 through Vin4 are all 750V, and the load is the four-channel rated load RL 10.5. The upper inverter output current ix1 of Channel 1 is not visible in Fig.6 due to the oscilloscope's limited number of measurement channels, but the waveforms and amplitudes of ix1 and ix2, ix3, and ix4 are nearly identical, with the exception of a little difference in phases (the phases of the four channels are not synchronized). The four-channel output voltage is somewhat different than the single channel's output voltage, which is 730 V, and the output power is 50.8 kW due to the tolerance between the components and coils. 97.0 percent is the calculated power loss distribution, and the measured dc-to-dc transfer efficiency.

 DOI : 10.35291/2454-9150.2022.0388

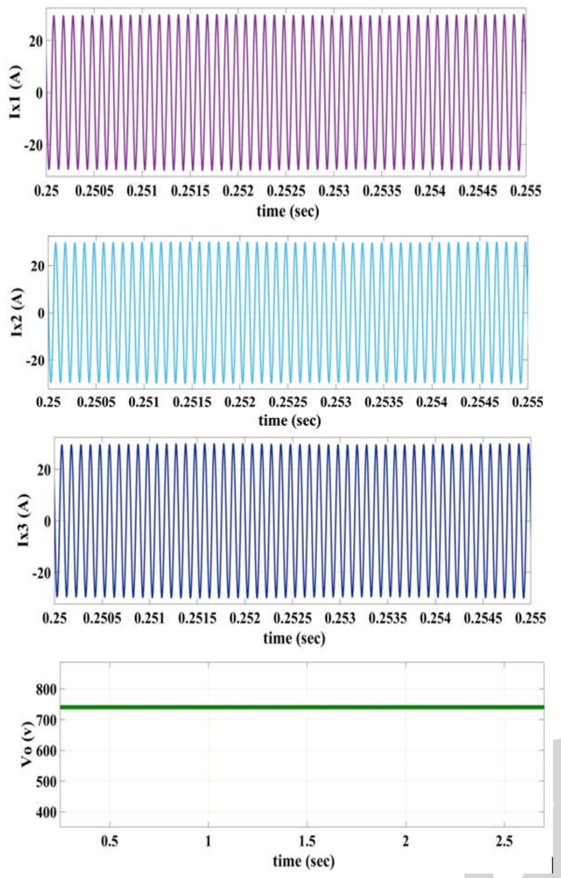

Fig. 7 Waveform when four channels are fully loaded (four-channel load RL 10.5 Ω).

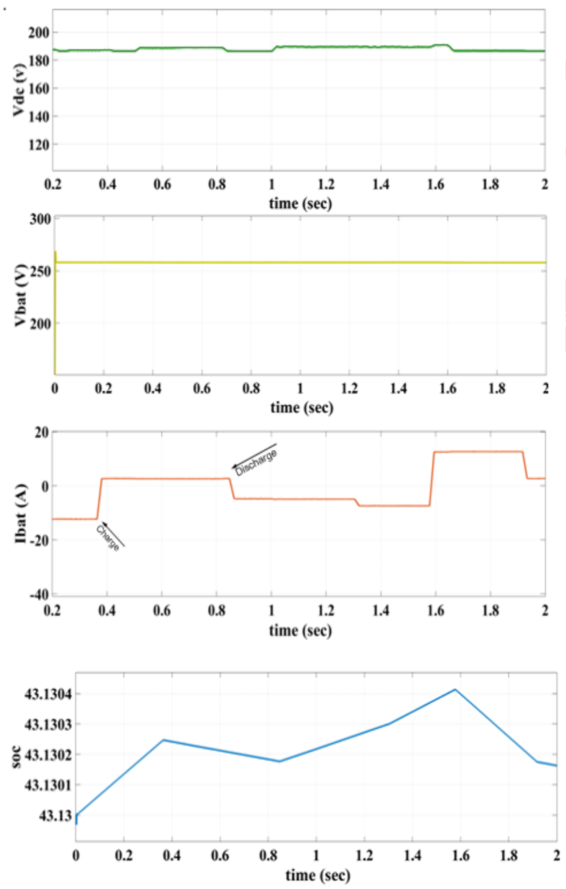

Fig. 8 Measured results by when four channels are in Battery charging and discharging mode.

VII.CONCLUSION

The ANFIS controller design is presented in this study for PWM-regulated ac/dc converters. The analysis given shows that the ANFIS application keeps system dampening. Simulation results show a quick transient responsiveness with fewer overshoots when compared to standard PI controller performance. A modular four-channel 50 kW WPT system with a decoupled coil design is available for rapid EV charging. The suggested scalable modular design allows the system to deliver 50 kW output power with low-power Silicon devices, greatly enhancing the system's dependability and robustness. The transmission power capabilities can be increased even further by adding more modules. An ANFIS controller created for For a 1kW/48V lithium polymer battery, all current loops have a bandwidth of more than 2 kHz, producing good on-road current emulation. Additionally advantageous for reducing charging current ripple and extending battery life is a high bandwidth current loop. A dynamic model of the current control loop is built by measuring and fitting the AC impedance and transfer function of a lithium polymer battery.

REFERENCES

[1] D. Patil, M. K. McDonough, J. M. Miller, B. Fahimi, and P. T. Balsara, ``Wireless power transfer for vehicular applications: Overview and challenges," IEEE Trans. Transport. Electri_c., vol. 4, no. 1, pp. 3_37, Mar. 2018.

[2] T. Trigg, P. Telleen, R. Boyd, F. Cuenot, D. D'Ambrosio, R. Gaghen, J. F. Gagné, A. Hardcastle, D. Houssin, A. R. Jones, and H. Kaneko, ``Global EV outlook: Understanding the electric vehicle landscape to 2020," Int. Energy Agency, vol. 1, pp. 1_40, Apr. 2013.

[3] J. H. Kim, B.-S. Lee, J.-H. Lee, S.-H. Lee, C.-B. Park, S.-M. Jung, S.-G. Lee, K.-P. Yi, and J. Baek, ``Development of 1-MW inductive power transfer system for a high-speed train," IEEE Trans. Ind. Electron., vol. 62, no. 10, pp. 6242_6250, Oct. 2015.

[4] A. Foote and O. C. Onar, ``A review of high-power wireless power transfer," in Proc. IEEE Transp. Electri_c. Conf. Expo (ITEC), Chicago, IL, USA, Jun. 2017, pp. 234_240.

[5] J. M. Miller and A. Daga, ``Elements of wireless power transfer essential to high power charging of heavy duty vehicles," IEEE Trans. Transport. Electri_c., vol. 1, no. 1, pp. 26_39, Jun. 2015.

[6] H. Hao, G. A. Covic, and J. T. Boys, ``A parallel topology for inductive power transfer power supplies," IEEE Trans. Power Electron., vol. 29, no. 3, pp. 1140_1151, Mar. 2014.

[7] J. Pries, V. P. N. Galigekere, O. C. Onar, and G.-J. Su, ``A 50-kW threephase wireless power transfer system using bipolar windings and series resonant networks for rotating magnetic _elds," IEEE Trans. Power Electron., vol. 35, no. 5, pp. 4500_4517, May 2020.

[8] V. P. Galigekere, J. Pries, O. C. Onar, G.-J. Su, S. Anwar, R. Wiles,L. Seiber, and J. Wilkins, ``Design and implementation of an optimized 100 kW stationary wireless charging system for EV battery recharging," in Proc. IEEE Energy Convers. Congr. Expo. (ECCE), Portland, OR, USA, Sep. 2018, pp. 3587_3592.

 DOI : 10.35291/2454-9150.2022.0388

[9] R. Bosshard and J. W. Kolar, ``Multi-objective optimization of 50 kW/85 kHz IPT system for public transport," IEEE J. Emerg. Sel. Topics Power Electron., vol. 4, no. 4, pp. 1370_1382, Dec. 2016.

[10] Y. Li, R. Mai, M. Yang, and Z. He, ``Cascaded multi-level inverter based IPT systems for high power applications," J. Power Electron., vol. 15, no. 6, pp. 1508_1516, Nov. 2015.

[11] B. X. Nguyen, D. M. Vilathgamuwa, G. Foo, A. Ong, P. K. Sampath, and U. K. Madawala, ``Cascaded multilevel converter based bidirectional inductive power transfer (BIPT) system," in Proc. Int. Power Electron. Conf. (IPEC-Hiroshima, ECCE ASIA), Hiroshima, Japan, May 2014, pp. 2722_2728.

[12] H. R. Rahnamaee, U. K. Madawala, and D. J. Thrimawithana, ``A multilevel converter for high power-high frequency IPT systems," in Proc. IEEE 5th Int. Symp. Power Electron. Distrib. Gener. Syst. (PEDG), Galway, Ireland, Jun. 2014, pp. 1_6.

[13] H. R. Rahnamaee, D. J. Thrimawithana, and U. K. Madawala, ``MOSFET based multilevel converter for IPT systems," in Proc. IEEE Int. Conf. Ind. Technol. (ICIT), Busan, South Korea, Feb. 2014, pp. 295_300.

[14] Q. Deng, P. Sun,W. Hu, D. Czarkowski, M. K. Kazimierczuk, and H. Zhou, ``Modular parallel multi-inverter system for high-power inductive power transfer," IEEE Trans. Power Electron., vol. 34, no. 10, pp. 9422_9434, Oct. 2019.

[15] D. Ahn and S. Hong, ``Effect of coupling between multiple transmitters or multiple receivers on wireless power transfer," IEEE Trans. Ind. Electron., vol. 60, no. 7, pp. 2602_2613, Jul. 2013.

[16] R. Johari, J. V. Krogmeier, and D. J. Love, ``Analysis and practical considerations in implementing multiple transmitters for wireless power transfer via coupled magnetic resonance," IEEE Trans. Ind. Electron., vol. 61, no. 4, pp. 1774_1783, Apr. 2014.

[17] Y. Li, T. Lin, R. Mai, L. Huang, and Z. He, ``Compact double-sided decoupled coils-based WPT systems for high-power applications: Analysis, design, and experimental veri_cation," IEEE Trans. Transport. Electri_c., vol. 4, no. 1, pp. 64_75, Mar. 2018.

[18] T. Shijo, K. Ogawa, M. Suzuki, Y. Kanekiyo, M. Ishida, and S. Obayashi, ``EMI reduction technology in 85 kHz band 44 kW wireless power transfer system for rapid contactless charging of electric bus," in Proc. IEEE Energy Convers. Congr. Expo. (ECCE), Milwaukee, WI, USA, Sep. 2016, pp. 1_6.

[19] H. Liu, Q. Chen, G. Ke, X. Ren, and S.-C. Wong, ``Research of the input-parallel output-series inductive power transfer system," in Proc. IEEE PELS Workshop Emerg. Technol., Wireless Power (WoW), Daejeon, South Korea, Jun. 2015, pp. 1_7.

[20] E. Babaei and S. H. Hosseini, ``New cascaded multilevel inverter topology with minimum number of switches," Energy Convers. Manage., vol. 50, no. 11, pp. 2761_2767, Nov. 2009.

[21] C.-S.Wang, G. A. Covic, and O. H. Stielau, ``Power transfer capability and bifurcation phenomena of loosely coupled inductive power transfer systems," IEEE Trans. Ind. Electron., vol. 51, no. 1, pp. 148_157, Feb. 2004.

[22] G. B. Joun and B. H. Cho, ``An energy transmission system for an artificial heart using leakage inductance compensation of transcutaneous transformer," IEEE Trans. Power Electron., vol. 13, no. 6, pp. 1013_1022, Nov. 1998.

[23] Wireless Power Transfer for Light-Duty Plug-in/Electric Vehicles and Alignment Methodology, Standard J2954_202010, 2020. [Online]. Available: https://saemobilus.sae.org/content/j2954_202010

[24] A. Ahmad, M. S. Alam, and R. Chabaan, ``A comprehensive review of wireless charging technologies for electric vehicles," IEEE Trans. Trans- port. Electri_c., vol. 4, no. 1, pp. 38_63, Mar. 2018.

[25] N. Liu and T. G. Habetler, ``Design of a universal inductive charger for multiple electric vehicle models," IEEE Trans. Power Electron., vol. 30, no. 11, pp. 6378_6390, Nov. 2015.

[26] J. W. Kolar and F. C. Zach, ``A novel three-phase utility interface minimizing line current harmonics of high-power telecommunications rectifier modules," IEEE Trans. Ind. Electron., vol. 44, no. 4, pp. 456_467, Aug. 1997.

[27] Gucien Electric. LW1600/0.10S2.0M33 Data Sheet. Accessed: Aug. 21, 2022. [Online]. Available: http:///www.gucien.com

[28] Dawn Electronic. DTR Series Resonance Capacitor Data Sheet. Accessed: Aug. 21, 2022. [Online]. Available: http:///www.dawn-cap.cn

AUTHORS PROFILE

Dr.J.Srinu Naick received his B.E degree in Electrical & Electronics Engineering from Andhra University Vishakhapatnam AP, India in 2003 and M.Tech with Energetics from NIT Calicut, Calicut, and Kerala, India in 2007. Ph.D with power system from Achiryanagarjuna university in 2019 He is having 18 years of teaching and research experience. He is currently working as Professor in the Department of EEE, Chadalawada Ramanamma Engineering college(Autonomous), JNTUA, Tirupati, Andhra Pradesh, India. His areas of interest are in the Power systems Industrial Drives & FACTS Controllers.

K. Lakshmi Priyanka is an Under Graduate student studying IV B.Tech Electrical and Electronics Engineering from Chadalawada ramanamma engineering College, Tirupati , Chittoor, Andhra Pradesh, India. Her research interests include Power Electronics.

 DOI : 10.35291/2454-9150.2022.0388